Simultaneous velocity–density measurements of downslope density clouds

Maria-Eletta Negretti, Antoine Martin, Florence Naaim-Bouvet

Simultaneous velocity-density measurements of downslope density clouds

M.E. Negretti*, A.Martin

Univ. Grenoble Alpes, CNRS, Grenoble INP, LEGI, Grenoble, 38000, France

F. Naaim-Bouvet

Univ. Grenoble Alpes, INRAE, UR ETNA, Grenoble, 38000, France

Abstract

We present results from laboratory experiments of the downslope propagation of a finite volume released gravity current by means of combined PIV/PLIF measurements. The experimental data were used to estimate the global characteristics of the current, such as the propagation speed, the lateral surface and the buoyancy, revealing that thermal theory is a robust model that can predict such quantities properly, especially the models of Beghin et al. (1981); Maxworthy (2010) and the theoretical model of Dai (2013a). The collected data allowed also for the determination of the entrainment rates based on the turbulent fluxes instead using the variation of the volume flux, and the regions of entrainement/detrainment have been identified. The results support previous observations of the mechanism responsible for the buoyancy loss of the cloud and its consequent deceleration down the slope, as a large scale recirculation vortex at the back of the cloud. A very complex interior structure of the cloud is observed, with a large variety of turbulent processes taking place, such as the large-scale convectively unstable recirculation vortex at the scale of the current itself, the small-scale convectively unstable motions inside the head of the cloud and close to the bottom boundary and shear (Kelvin-Helmholtz) instabilities at the boundary between the current and the ambient water. The synoptic velocity and density measurements allowed also to test existent parametrizations of turbulent fluxes, that have been quantified in 2D fields with a high spatial resolution. Results confirm that parametrization laws based on the assumption of a constant turbulent diffusivity or mixing length do not apply for buoyancy clouds due to their high spatial heterogeneity. Hence, the parametrization of the turbulent dif-

*Corresponding author

Email addresses: eletta.negretti@legi.cnrs.fr (M.E. Negretti), antoine.martin@univ-grenoble-alpes.fr (A.Martin), florence.naaim@inrae.fr (F. Naaim-Bouvet)

fusivities in such flows should be based on scalar quantities that avoid the problem of spatial heterogeneity and takes into account the different sources of turbulence production, e.g. using energetic considerations that compare the terms having a definite exchange of energy and acts as a source or a sink.

Keywords: Gravity currents, mixing, experiments, sloping bottom, internal structure

1. Introduction

Variations in temperature, salinity and/or sediment concentration cause variations of fluid density in the vertical direction. The resulting flow stratification, which typically occurs in environmental and geophysical flows, leads to qualitative and quantitative modifications of the flow patterns by buoyancy. When buoyancy driven flows encounter topography, a downslope dense current, i.e. gravity current, is created. Its motion is then sustained by buoyancy and deviated by the topographic slope. Gravity currents are key processes that affect ocean, atmospheric and coastal circulation.

Gravity currents can take on different forms depending on their source of supply of buoyancy being continuous (Baines, 2002; Britter and Linden, 1980; Martin et al., 2019; Negretti et al., 2017; Odier et al., 2014) or resulting from a finite volume release (Beghin et al., 1981). Examples of the first type are oceanic gravity currents (Baringer and Price, 2001), while examples of finite volume released gravity currents are avalanches (Clément-Rastello, 2001; Hopfinger, 1983; Rastello and Hopfinger, 2004), volcanic eruptions (Holyer and Huppert, 1980) or turbidity currents (Meiburg and Kneller, 2010), which contribute to the shaping of the continental surface and have a large impact on the geomorphological floor and the related ecosystems (Bründl et al., 2010; Kostaschuk et al., 2018; Pohl et al., 2020; Thorez et al., 2021). Katabatic winds are also an example of an intermittent gravity flow and are important to determine the local air circulation in several regions (Brun, 2017; Charrondiere et al., 2020).

This paper deals with finite volume released gravity currents over sloping boundaries. For the terminology, finite volume released gravity currents on a sloping boundary is more precisely described as a 'thermal cloud' or 'density cloud' (Simpson, 1982), because the flow resembles more a cloud with some tail following.

The pioneering work on donwlope propagating density clouds was made

by Beghin et al. (1981), who studied the full range of slopes between 5° and 90°. They showed that the current development includes a first quick accelerating phase of the density cloud, followed by a decelerating phase, if no buoyancy is entrained by the current, as for gravity currents propagating over a sediment bed (Rastello and Hopfinger, 2004). Further theoretical, numerical and experimental studies followed, giving important insights in the dynamics and the spatio-temporal development of the current (Adduce et al., 2012; Beghin and Brugnot, 1983; Beghin et al., 1981; Dai, 2012, 2013a, 2014, 2015; Dai et al., 2011; Hopfinger, 1983; Martin et al., 2020; Ottolenghi et al., 2017; Rastello and Hopfinger, 2004; Steenhauer et al., 2017a; Zemach et al., 2019).

To describe the front velocity history of a lock-released gravity current both a shallow water model approach (Ross et al., 2002; Tickle, 1996; Ungarish, 2009; Webber et al., 1993) or thermal theory (Beghin et al., 1981; Morton et al., 1956) have been adopted. In the latter case, the assumption of a constant buoyancy flux during the head propagation was made and despite the strong approximation, this model has shown to give a good description of the evolution of both the first accelerating phase and the successive decelerating phase (Beghin et al., 1981).

A more sophisticated model has been proposed by Maxworthy and Nokes (2007), who argued that during the acceleration phase, the head was being fed by a following current that increased its buoyancy as it propagated downstream. Maxworthy (2010) showed that after a propagation distance of the order of (5–10)H_0, where H_0 is the initial depth of the lock, the inflow into the rear stopped, and the head began to lose buoyancy-containing fluid from its rear by the detachment of large, weakly vortical structures. Their measurements have shown that the buoyancy in the current head increased during the acceleration phase and decreased during the deceleration phase.

Dai (2012, 2013b) implemented a three-dimensional direct numerical simulation of a lock released downslope gravity current. They confirmed numerically that the maximum buoyancy in the head never reaches the total released buoyancy, and a significant portion of heavy fluid is left in the tail current, which is often detached from the head when the density cloud propagates over steep slopes (see also Dai (2013a,c)), in accord with Maxworthy (2010). For a long running length $x > 13H$, they showed a disagreement between the thermal theory (Morton et al., 1956) and the observed growth of the density cloud in the deceleration phase.

Recently, Martin et al. (2020) and Zemach et al. (2019) proposed a the-

oretical solution based on the shallow water model combined with a Benjamin's type jump condition at the nose of the head and an empirical entrainment law, respectively. Their solution is of relevance during the acceleration phase only, taking into account the contribution of the tail to the buoyancy budget of the density cloud, as reported by Maxworthy and Nokes (2007). However, the model cannot predict the loss of buoyancy in the deceleration phase (Dai, 2012, 2013a; Maxworthy, 2010).

While previous studies mostly concentrated on the global properties of such density clouds propagating on horizontal or inclined boundaries, their internal structure has started to receive attention only recently. Hopfinger and Tochon-Danguy (1977) measured the velocity distribution within the density cloud by means of the hydrogen bubble technique combined with a conductivity probe measurement for the density. Three-dimensional direct numerical simulations of a lock-released gravity current were performed by Calgaro et al. (2015); Étienne et al. (2004); Steenhauer et al. (2017b) revealing a very turbulent structure of the buoyancy cloud. Nishimura and Ito (1997) measured internal velocities of 50 ms^{-1} for a front velocity of about 10 ms^{-1}, demonstrating that the head interior is characterized by a strong energetic circulation and a large variety of turbulent structures. Knowing the internal structure of density clouds may help to better predict the entrainment and dilution mechanisms, which are directly related to the propagation speed and motion of such currents.

Detailed velocity and/or density measurements within the head of a density cloud propagating over a horizontal boundary using optical non-intrusive measurements techniques (such as Particle Image Velocimetry-PIV) have been performed only in few studies (Hallworth et al., 1996; Martin and García, 2009; Pelmard et al., 2021; Thomas et al., 2003). Hallworth et al. (1996) and later Martin and García (2009) observed the formation of persistent Kelvin–Helmholtz type billows at the front of the density current causing entrainment of ambient fluid into the current at the interface current/ambient.

Here, we performed experiments on finite volume released gravity currents over steep sloping boundaries (with slope angles of 15° and 20°) using simultaneous PIV/PLIF measurements techniques. Such measurements in unsteady and heterogeneous turbulent buoyancy flows are rare, but are very useful since they allow to highly resolve both large-scale and small-scale flow motions and statistics, which otherwise are very difficult to measure. This also enables resolving turbulent fluxes and their spatial distribution, which

are impossible to quantify with other measurement techniques.

The recent studies performed by Agrawal et al. (2021); Mukherjee and Balasubramanian (2020, 2021) on horizontal lock-released gravity currents focused on the slumping phase and their analysis was aimed at estimating the mixing efficiency at the interface between the cloud and the ambient fluid due to Holmboe or Kelvin-Helmholtz instabilities. No study is known in the literature on downslope density clouds aimed at verifying the theories of the global characteristics governing the dynamics of such flows, as the front propagation, the buoyancy and the entrainment, but also quantifying small-scale processes and turbulent fluxes that characterize the internal structure of the density cloud, based on highly resolved simultaneous measurements of both the velocity and the density fields. By means of such detailed measurements, the validity and limitations of the existent theories for both the global characteristics of the flow, but also those related to the parametrization of the turbulent diffusivities, have been tested, revealing interesting insights on the small-scale features of the internal structure of the head. The global characteristics of the density cloud compared to the semi-empirical thermal theory of Beghin et al. (1981) and Escudier and Maxworthy (1973) reveal a fairly good agreement, with exception of the assumption of initial mass conservation, in accord with Maxworthy (2010). The predictions for the buoyancy loss of the gravity current during the decelerating phase are in better agreement with the theoretical model proposed by Dai (2013a,c), while the model of Maxworthy (2010) reveals to strongly overestimate it, even if the trend of decrease is well represented by Maxworthy (2010)'s theory

A very complex interior structure of the buoyancy cloud is observed, with a variety of turbulent processes sources of mixing and dilution present. These are large-scale and small-scale convective motions inside the cloud, shear turbulence and related instabilities (e.g. Kelvin-Helmholtz and boundary layer instabilities) at the boundaries with the ambient fluid and the bottom. Finally, it is shown that classical mixing parametrizations of turbulent fluxes based on mixing length models are not appropriate for lock-released buoyancy clouds due to their strong spatial and temporal heterogeneity.

The paper is organized as follows: section 2 outlines the experimental set-up and the measurement techniques. Section 3 gives the global characteristics of the buoyancy cloud, while entrainment/detrainment and mixing are presented in 4 and 5, respectively, and compared to existent parametrizations. Section 6 summarizes the results and includes concluding remarks.

2. Experimental facility and measurement techniques

2.1. Experimental setup

The experimental set-up is shown schematically in figure 1a. A plexiglas water channel 2.76 m long, 20 cm wide and 38cm deep was immersed in a larger water tank of dimensions 2.4 $m \times 2.4\ m \times 2.4\ m$. The slope angle of the experimental channel was set to the desired angle. The dense fluid was introduced in a reservoir $L_0 = 20\ cm$ long and 30 cm deep, with a lock depth of $H_0 = 6.25cm$ located at the upper end of the channel and initially separated by a removable gate, resulting in an initial lateral surface of $A_0 = L_0 \times H_0 = 125cm^2$. The initial reduced gravity was fixed to $g'_0 = g\Delta\rho/\rho_a = 5cm/s^2$ and produced by saline solutions with $\Delta\rho = 5.1 \pm 0.1\ kgm^{-3}$ and a constant temperature of $19.7°C\ \pm 0.1$, measured just before each experiment with a high precision (10^{-3}) densimeter (DMA TM 35, Anton Paar). The resulting Reynolds numbers were $\mathrm{Re} = UH/\nu \approx 1.2 \cdot 10^4$ where U and H are respectively the typical velocities and depths of the cloud in the measurement region and ν the kinematic viscosity.

Run	A_0 [cm^2]	$\theta[°]$	$g'_0[cm/s^2]$	N	Technique	F.O.V.
1	125	15	5 ± 0.1	5	PIV/PLIF	$1.65m < x < 2.5m$
2	125	20	5 ± 0.1	7	PIV/PLIF	$1.65m < x < 2.5m$
3	125	15	5 ± 0.1	5	PIV/PLIF	$0.7m < x < 1.55m$

Table 1: Main parameters of the experimental runs.

Two runs of experiments have been performed in the deceleration region $1.65m < x < 2.5m$ from the lock release (see figure 1). The same initial conditions have been adopted for both runs with exception of the bottom slope, which was set to 15° in the first run and 20° in the second run of experiments. A third run of experiments has been conducted in the initial stage of the decelerating region within $0.7m < x < 1.55m$ from the lock release, and same initial conditions as in the first run of the experiments. The same experiment was repeated $N \leq 7$ times to check for reproducibility and all calculated quantities have been averaged over the N experiments (ensemble average). The main parameters of the experimental runs are summarized in table 1. For all runs, synoptic PIV and PLIF measurements techniques have been used to capture simultaneously the velocity and density fields, respectively. Essential details are given below and in the appendix.

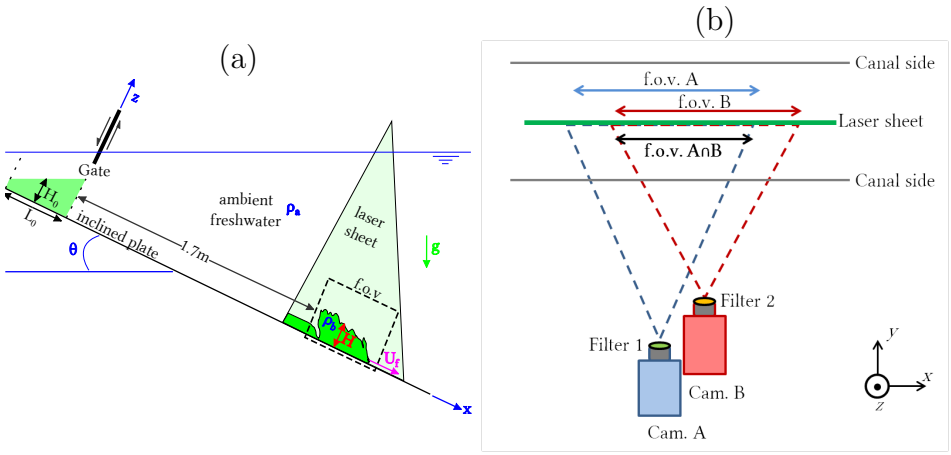

Figure 1: (a) Side view of the experimental setup. (b) Top view of the optical measurement configuration for PIV and PLIF.

2.2. Measurement technique

The velocities and the density were determined using the optical, non-intrusive experimental techniques of Particle Image Velocimetry (PIV) and Planar Laser-Induced Fluorescence (PLIF), respectively. Both PIV only and combined PIV/PLIF experimental data are used in the following results sections. Essential details on the measurements techniques are given below, while the detailed procedure for the PLIF calibration is given in the appendix.

The PIV set-up consisted of a light source, light sheet optics, seeding particles, a camera, and a PC equipped with a frame grabber and image acquisition software. Polyamide particles (Orgasol) with a mean diameter of 60μm and a specific density of 1.016g/cm^{-3} were added in both the fresh water and the salt water in the initial release reservoir as tracer material for the PIV measurements.

A 5 Watt Yag-laser ($\lambda = 532$ nm) has been used as continuous light source. The beam was transmitted through mirrors to a spherical lense with an angle of 45° to generate a laser sheet with a length of approximately 1 m and a width of 5mm, positioned in the middle of the channel. Rhodamine 6G was used as fluorescent dye (absorption peak at 530nm and emission peak at 555nm) and uniformly mixed in the reservoir containing the dense fluid with initial concentration $c_0 = 5\mu g/l$. The dye and the salt have approximately

the same diffusivity, with a Schmidt number $Sc = \nu/\kappa = 700$, where κ is the mass transfer diffusion coefficient (Troy and Koseff, 2005).

For the simultaneous PIV/PLIF measurements an interferometer band-pass, 532nm for PIV and a high pass filter with cut-off 550nm for PLIF were used to separate the emitted wavelengths.

Images of roughly 70cm $\times$ 55cm were grabbed with a CCD camera (Flow Master 1200×1600 pixels) for PIV, and with a second CCD camera (Dalsa 1000×1000 pixels) at a frame rate of 23.22 Hz for PLIF.

The raw image pairs were then processed using a PIV cross-correlation algorithm (software package DaVis, LaVision) to compute the velocity fields, starting with an interrogation window of 32×32 pixels and a final window size of 16×16 pixels with 50% overlap. Each vector of the resulting vector field represents an area of roughly $0.6cm \times 0.6cm$. Given the velocities encountered in the experiments, the error for the instantaneous velocity is approximately 4%.

The calibration procedure for the PLIF measurements is given in the appendix.

3. Experimental results

3.1. Global characteristics of the density cloud

Figure 2 illustrates an instantaneous side view of a calibrated density field. The cloud has the size of the present PIV/LIF field of view, hence, present results are treated in terms of the vertical coordinate z and time t, where time is converted in the streamwise space coordinate x by neglecting the time distortion of the cloud during the advective time t_A at a given x-position, and assuming a constant advective velocity of the cloud over this time laps.

For each x-position, the density cloud is detected (t, z) using a threshold of $0.99(\Delta\rho/\rho)_{max}$ for the density.

As suggested by Beghin et al. (1981), and as evident from present visual observations, the shape of the cloud can be fitted in time and vertical space (t, z) assuming a semi-elliptic shape (cf. also figure 5), that follows the following equation

$$z = \frac{H}{0.5t_A} \left((0.5t_A)^2 - (t - t_0)^2 \right)^{\frac{1}{2}}, \tag{1}$$

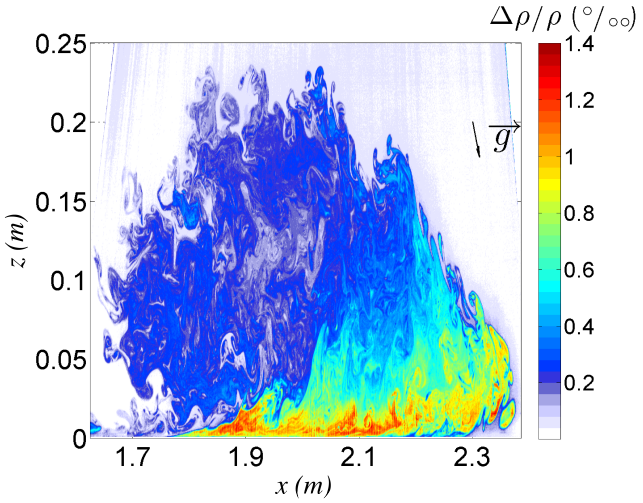

Figure 2: Instantaneous density field of the cloud for $[\Delta\rho/\rho]_i = 5 \cdot 10^{-3}$ and run 2 (cf. table 1).

where z is the vertical (normal to the slope) coordinate of the boundary of the density cloud with the ambient fluid, H and $0.5t_A$ are the minor and major axis of the ellipse and t_0 is the time corresponding to a given position of the geometrical centre of the ellipse x_g. From equation (1), H and the length $L = t_A U$ of the density cloud can be estimated, where U is the velocity of the geometric centre of the ellipse defined as

$$U = \frac{\Delta x}{\Delta t_0} \tag{2}$$

Figure 3a, shows the non-linear fit using equation (1) (dashed line) compared to experimental values (solid line). The streamwise coordinate corresponds to the dimensionless advective time $(t - t_0)/t_A$, where t_0 has been determined using a power law fit ((Beghin et al., 1981), cf. figure 3b).

Using this procedure, the velocity of the buoyancy cloud U, its surface area A and its buoyancy flux $B = g'UH$ have been determined.

Figure 4a shows the normalized experimental velocity $U/\sqrt{g'_0 H_0}$ (solid line) obtained from equation (2) clearly in the deceleration stage and in good accord with predictions of the thermal theory (dashed line).

The normalized lateral surface A/A_0, defined as $A = \frac{\pi}{4}LH$, where L and H are estimated from equation (1), is shown in figure 4b. Beghin et al. (1981)

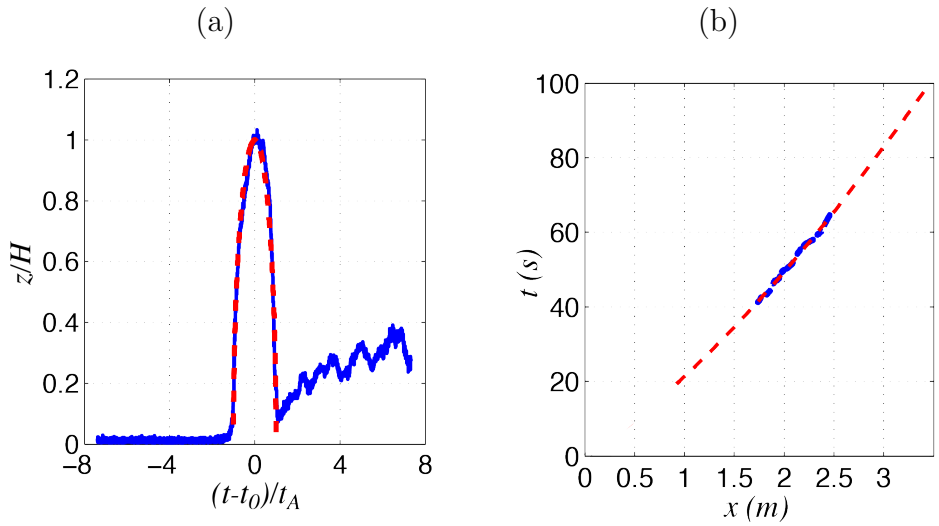

Figure 3: (a) Nonlinear fit of the shape of the buoyancy cloud by a half-ellipse (run 1). Dimensionless height of the cloud (blue line); Dimensionless fit (red dashed-line). Horizontal axis corresponds to a dimensionless advective time and the vertical axis corresponds to the dimensionless height. (b) Time position t_0 of the geometric center of the ellipse function of the along slope position (blue line). The dashed line is deduced from a fit by a power law following Beghin et al. (1981).

showed experimentally that the surface of the buoyancy cloud increases with the square of the along slope direction as $A = C\,(x + x_0)^2$, where C is a constant defined as $C = \pi/16\,(S_2/S_1)^2\,\alpha^2$ and x_0 is a virtual origin corresponding to $A = 0$, i.e. $x_0 = 4S_1/S_2\alpha^{-1}\sqrt{A_0/\pi}$. The shape factors S_1 and S_2 are estimated assuming a semi-elliptical shape of the buoyancy cloud, and α is an empirical entrainment coefficient (see also equation 7). This model is represented by a dashed line in figure 4b revealing a good agreement with the experimental data in the initial accelerating stage. At $X/L_0 \sin\theta \approx 2.8$, corresponding to $x \approx 34H_0$, the data suggests that the lateral surface stops increasing, in accord with previous numerical observations (Dai, 2012, 2013b; Steenhauer et al., 2017b). In particular, for a slope of 10°, Dai (2012) observed that the semi-elliptical head experiences multiple sporadic reductions in its height.

As mentioned in the introduction, Maxworthy (2010) explained this behaviour as the result of loss of volume (and buoyancy) that takes place during the descent, induced by large scale vortical structures developing at the back of the gravity current head, that has been also supported by Dai (2013a,b).

The numerical results from Dai (2013b) are also reported as symbols in figure ??b: results are within the range of our data and the theoretical prediction of Maxworthy (2010); however, the lateral surface A increases monotonically and no decrease is observed.

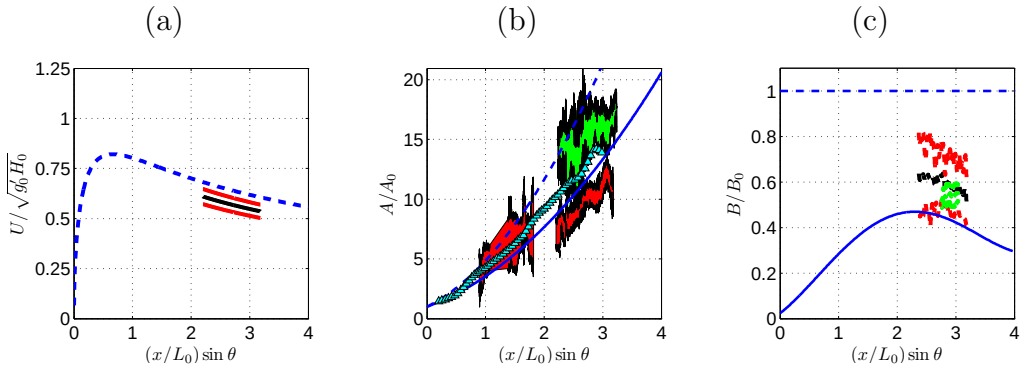

Figure 4: Experimental global characteristics of the buoyancy cloud with $Re \approx 1.2 \times 10^4$ (a) Velocity of the geometrical center U from equation (2) of the buoyancy cloud (runs 1 and 2). (b) Lateral surface of the buoyancy cloud function of the along-slope direction for run 1 with a slope of 15° (red shaded region) and run 2 with a slope of 20° (green shaded region), and from DNS of Dai (2013b) (symbols). The x axis has been re-normalized by $L_0/\sin\theta$.(c) Dimensionless experimental ensemble average of the buoyancy of the cloud B from equation (3) (black line) and B' from equation (4) (green line). Red lines represent the confidence interval. The blue dashed and continuous lines represent the empirical equation from Beghin et al. (1981) and from Maxworthy (2010) respectively, where the x axis has been rescaled by $L_0/\sin\theta$.

Figure 5, illustrates the density field at three different x positions. In (a), at $x_g = 2.2\ m$, the buoyancy cloud is well fitted by the half-elliptic shape, with a very active back vortex incorporating ambient water at the back of the cloud. On figure 5(b), at $x_g = 2.3\ m$, a larger interfacial shear instability develops which begins to separate the back of the cloud, as seen later in (c): there is clearly a loss of volume and mass at the back of the cloud. This phenomenon is observed in all the experiments, although with variable intensity, and confirms the suggestion of Maxworthy (2010) and Dai (2013a) to explain the observed decrease of buoyancy in the second stage of propagation of the cloud down the slope.

Steenhauer et al. (2017) observed a variation in the development of the lateral surface at $x \approx 35H_0$ for slopes larger than 30°. They showed that for sufficiently large distances from the source, the normalized sub-volume

containing mixed fluid (which is linearly related to the lateral surface A) starts decaying for any value of the slope θ related to a strong dilution of the sub-volume. Defining a constant, C_0 representing the ratio between mixed and unmixed fluid, they observed that smaller values of C_0 corresponded to extended regions in which the lateral surface A increases linearly with x and trends in the variation of A with x are similar for any value of C_0.

The buoyancy of the semi-elliptical cloud is shown in figure 4c, defined as

$$B = U \int_0^{\infty} \left(\int_{t_N}^{t_B} g' \delta_c dt \right) dz, \tag{3}$$

where t_N and t_B are respectively the time at a given distance x at which the nose and the back of the ellipse appears, respectively, and δ_c is the Dirac function. Note that this definition of the buoyancy differs from that of Maxworthy (2010) by a factor of $1/\rho_0$, which is cancelled out in figure 4c since it is normalized with the initial buoyancy. From the figure, it emerges that at $(x/L_0)\sin\theta = 2.2$ the buoyancy of the cloud is about 60% of the initial buoyancy, demonstrating that during the descent buoyancy has been left behind in the tail. For this value of the buoyancy, thermal theory predicts a velocity 84% of the predicted velocity, which explains the lower velocity (88%) reported in figure 4a. For comparison, we also report the conservation of buoyancy from Beghin et al. (1981) (dashed line in figure 4c). Maxworthy and Nokes (2007) and Maxworthy (2010) showed that the buoyancy of the cloud is not conserved in the deceleration stage of the density cloud. For a slope angle of 10.6°, they showed that the buoyancy of the cloud reaches a maximum of about $43\%B_0$ for $x \approx (10-13)H_0$ and decreases afterwards. This is represented as a continuous line in figure 4c and we see that the descent of our data follows the trend of Maxworthy (2010).

The theoretical solution of Maxworthy (2010) however underestimates our reported values (60% versus 43%), which may be imputed by the different definition of the buoyancy threshold within the cloud or by the different quantities used for its estimation: in our case the buoyancy has been obtained by instantaneous velocity and density measurements, and not from dye concentration measurements.Dai (2013a) derived a power-law relationship which enables to estimate the fraction of heavy fluid in the lock that is contained within the head, χ, via $\chi = [K_M/K_B]1^3$, where K_M is parameter which has been determined by several measurements in previous studies (Beghin et al. (1981), Hoult (1972), Huppert and Simpson (1980), Marino et al. (2005)),

whereas a theoretical derivation of K_B is given in Dai (2013a) (cf. equation (1.7) therein). The theoretical estimations of Dai (2013a) were also in good agreement with the measurements of Beghin et al. (1981), predicting values of ≈ 0.75 for slope angles below 5° and ≈ 0.82 for slope angles of 9° (Dai, 2013c). These values are much higher than those predicted by Maxworthy (2010) and this difference was explained by erroneous estimations of the model constant K_B and/or a different definition of the head dye concentration threshold. If we estimate the model constant with our values using equation (1.7) in Dai (2013a), we obtain $K_B = 3.8$, resulting in $\chi \approx 0.63$ for $K_M = 2.45$ (Beghin et al., 1981), which is in good agreement with the reported values in figure 4c of 0.6.

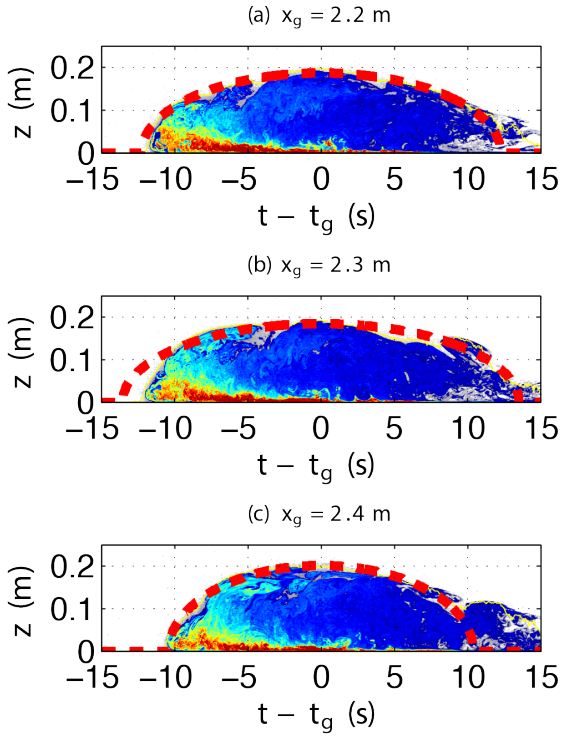

Figure 5: Density field at three different x positions for run 1. Non-linear fit of the shape of the buoyancy cloud using a half-ellipse (red dashed line). Horizontal axis corresponds to the advective time.

In order to assure that the results do not depend on the definition chosen to determine the buoyancy of the cloud, it has also been estimated directly

using the combined PIV/PLIF data as follows

$$B' = \int_0^{\infty} \left(\int_{t_N}^{t_B} u(z,t) g' \delta_c dt \right) dz = B \frac{U_m}{U}, \tag{4}$$

where $u(z,t)$ is the local velocity from the PIV and U_m the velocity of the centre of mass of the buoyancy cloud. The buoyancy B' is shown in figure 4c as a green line, revealing that both estimations for B and B' give similar results: the ensemble average of B' is slightly smaller than that of B because the geometric velocity U overestimates the velocity of the centre of mass of the cloud.

3.2. Interior structure

Figures 6 (a,b) show the mean structure of the buoyancy cloud with the black arrows representing the velocity difference between the ensemble average of the instantaneous velocity $\langle \vec{u} \rangle$ and the ensemble average of the velocity of the gravity center $\langle \vec{u}_B \rangle$ of the buoyancy cloud. The density for $[\Delta\rho/\rho]_i = 5 \times 10^{-3}$ in (a) and the mean vorticity ($\omega_y = \frac{\partial u}{\partial z} - \frac{\partial w}{\partial x}$) in (b) are highlighted by the colormaps.

Clearly, the density within the cloud is not homogeneous and at the back of the head, a large-scale vortex appears, associated to a downward vertical velocity at the outer edge of the density cloud and an upward vertical velocity in the central area of the head, with evident regions convectively unstable (cf. colormap in figure 6a). Such a large scale vortex structure has been already observed in the literature (e.g. Beghin and Brugnot, 1983; Dai, 2013a; Hampton, 1972). This vortex is composed of much lighter water ($\approx 4\% g'_0$) as compared to the frontal part at the nose ($\approx 12\% g'_0$), entrained from the ambient. The size of the large-scale vortex is of the order of the maximum depth of the buoyancy cloud. The averaged reduced gravity within the cloud is about $6\% g'_0$, thus 60% of the initial value, during the considered space-time interval when observations were taken.

Figure 6(b) shows that the vorticity is negative at the interface between the buoyancy cloud and the ambient water and positive in the bottom boundary layer of the buoyancy cloud. The high values of the vorticity on the back of the buoyancy cloud confirms the presence of the large-scale vortex. High positive vorticity is observed at the nose of the buoyancy cloud, highlighting the presence of Kelvin-Helmholtz like structures on the frontal part of

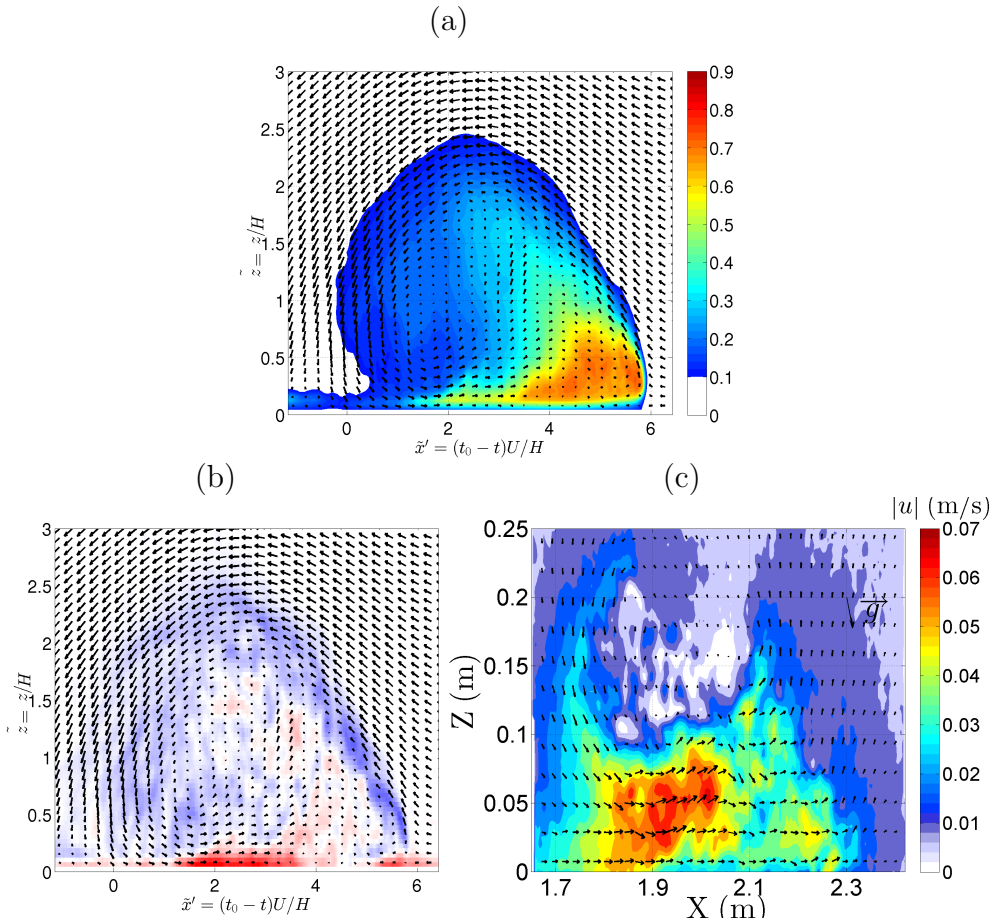

Figure 6: Mean structure of the buoyancy cloud for run 2 with the velocity $\langle \vec{u} \rangle - \langle \vec{u}_B \rangle$ (black arrows) and $\langle \vec{u}_B \rangle$ being the velocity of the gravity center of the buoyancy cloud. The density for $[\Delta\rho/\rho]_i = 5 \times 10^{-3}$ in (a) and the mean vorticity ($\omega_y = \frac{\partial u}{\partial z} - \frac{\partial w}{\partial x}$) in (b) are highlighted by the colormaps. (c) Snapshot of an instantaneous PIV/PLIF field.

the head (Martin and García, 2009) and at the outer boundary of the large-scale vortex within the buoyancy cloud, induced by enhanced vertical shear generated by the vortex itself.

These results also highlight that a variety of different turbulent processes take place inside the density cloud: the large-scale and small-scale convective motions which become locally unstable in the core of the cloud, shear turbulence as Kelvin-Helmholtz instabilities at the boundary with the ambient fluid, as also observed and quantified by Balasubramanian and Zhong (2018),

and boundary layer instabilities at the bottom boundaries, which all concur to the dilution of the cloud.

4. Entrainment

Two phenomena responsible for entrainment can be distinguished (cf figure 6): the first is induced by the large scale vortex (of typical scale of the order of H) that engulfs ambient water within the full cloud, and the second is due to small scale (shear) instabilities of typical scale of the order of ≈ 1 cm that develop at the contours of the buoyancy cloud with the ambient water and entraining locally.

The conservation of mass for the buoyancy cloud can be expressed using the model of the thermal theory considering the temporal variation of the lateral surface A:

$$\frac{DA}{Dt} = \alpha U \Gamma, \tag{5}$$

where $\alpha = -W/U$, is the entrainment coefficient, W is the average entrainment velocity across the contour Γ corresponding to the buoyancy cloud interface with the ambient water, assuming a 2D flow. This formulation neglects the variations of density, that can be assumed valid for small $\Delta\rho/\rho$. More rigorously, the conservation of mass across the control volume representing the density cloud, can be expressed as

$$\frac{D}{Dt}\iint_{S_\Gamma} \rho ds = \iint_{S_\Gamma} \vec{\nabla}_P \cdot (\rho\vec{u})\, ds + \iint_{S_\Gamma} \rho \partial_y v ds, \tag{6}$$

where $\vec{\nabla}_P \cdot \vec{u} = \partial_x u + \partial_z w$ is the divergence of the velocity in the (x, z) plane. Assuming the flow to be primarily two-dimensional, the last term on the right hand side of equation (6) can be neglected, so that the local mass flux can be directly estimated across the interface between the buoyancy cloud and the surrounding ambient. The entrainment coefficient α used in the thermal theory can be then written as

$$\alpha = \frac{1}{\rho_0 U}\oint_\Gamma \rho\vec{u}\cdot\vec{n}dl \Big/ \oint_\Gamma dl = \frac{1}{\rho_0 U C}\oint_\Gamma \rho\vec{u}\cdot\vec{n}dl, \tag{7}$$

where the circulation integral in the latter equation can be replaced by the surface integral using the Green's theorem

$$\oint_\Gamma \rho\vec{u}\cdot\vec{n}dl = \iint_{S_\Gamma} \vec{\nabla}_P \cdot (\rho\vec{u})\, ds. \tag{8}$$

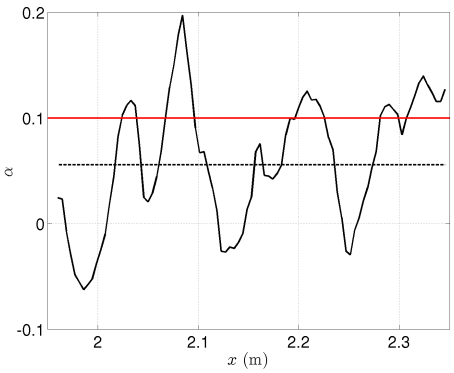

Figure 7: Entrainment coefficient. Coefficient deduced from equations (7) and (8) (black line) and its spatial average (horizontal dashed line); constant coefficient proposed by Beghin et al. (1981) (horizontal red line).

Figure 7 displays the entrainment coefficient deduced from equations (7) and (8). The observed sign fluctuations of α in figure 7 are of the order of the spatial average (cf. dashed line in figure 7) and correspond to entrainment (positive) and detrainment (negative). For comparison, the constant entrainment coefficient proposed by Beghin et al. (1981) is also reported (continuous line).

Odier et al. (2012) suggested a quantitative measure of local entrainment and detrainment derived from observed conditional correlations of density fluxes to fluctuations of density ρ' or of the vertical velocity w'.

Figure 8 shows the two-dimensional probability density functions (PDF) of ρ' versus $\rho' w'$ for the initial development phase where the lateral surface of the buoyancy cloud increases (a) and for the second stage characterized by a decreasing lateral surface of the buoyancy cloud (b). The right part of the plots corresponds to the stabilizing return to neutral buoyancy, while the top left quadrant corresponds to entrainment, and the bottom left quadrant to detrainment. It is evident comparing the two figures, that most of the entrainment takes place in the initial development phase of the density cloud, while detrainment is dominant during the second phase characterized by the detachment of the back of the cloud.

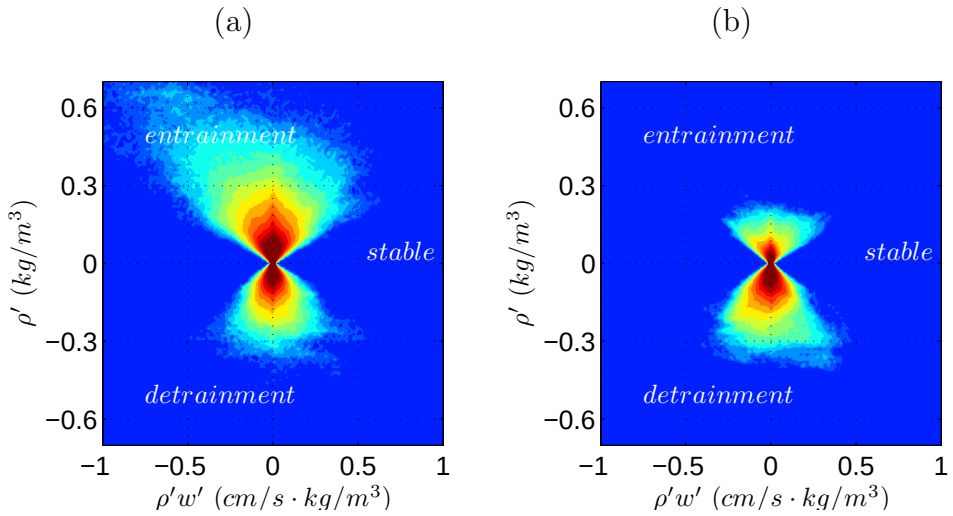

Figure 8: Two-dimensional PDFs of the density flux versus the density fluctuations. (a) During the increasing phase of A/A_0 (run 3). (b) During the decreasing phase of A/A_0 (runs 1 and 2.

5. Turbulent fluxes

The results in section 3 have shown that a variety of turbulent motions characterize the internal structure of the density cloud. Turbulent motions are usually not solved explicitly in numerical models and thus they need to be parameterized (e.g. Madec, 2015).Vertical turbulent fluxes are generally assumed to depend linearly on the gradients of large-scale quantities.

The eddy viscosity ν_t is used in the momentum equation to parameterize the Reynolds stress such as:

$$\langle u'w' \rangle = -\nu_t \left\langle \frac{\partial u}{\partial z} \right\rangle \tag{9}$$

A frequently used turbulence closure for mixing in ocean or atmospheric circulation models is to assume a linear relation between the vertical buoyancy flux and the density gradients. This relation defines a diapycnal turbulent diffusivity K_ρ that can be written as

$$\langle \rho'w' \rangle = -K_\rho \left\langle \frac{\partial \rho}{\partial z} \right\rangle \tag{10}$$

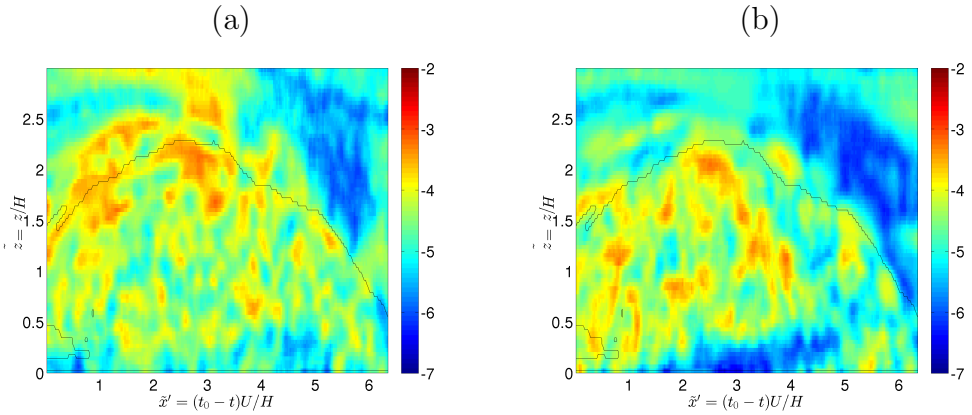

Figure 9: Turbulent diffusivity ($log_{10}\mathrm{m}^2/\mathrm{s}$) in the buoyancy cloud. ν_t (a); K_ρ with stable stratification (b).

Maps of the turbulent diffusivities are shown in figure 9, with ν_t in (a) and K_ρ in (b). ν_t and K_ρ present the same order of magnitude, with high values ($> 10^{-4}$ $\mathrm{m}^2\mathrm{s}^{-1}$) within the large-scale vortex and smaller values ($< 10^{-5}$ $\mathrm{m}^2\mathrm{s}^{-1}$) close to the nose and at the bottom. Their spatial structure is however different. Turbulent diffusivities ν_t are intensified at the edge of the large-scale vortex and the ambient, whereas diapycnal turbulent diffusivities K_ρ present the largest values in the core of the large-scale vortex. These estimations show clearly that the usual hypothesis of a constant diffusivity for the entire density cloud does not apply, with strong variations of one order of magnitude.

Prandtl (1925) proposed a mixing length scale $\mathcal{L}_u$ to relate the Reynolds stress and the square of the mean velocity vertical shear:

$$\langle u'w' \rangle = \mathcal{L}_u^2 \left\langle \frac{\partial u}{\partial z} \right\rangle^2 \tag{11}$$

Similarly, for the buoyancy flux a buoyancy mixing length $\mathcal{L}_\rho$ can be defined:

$$\langle \rho'w' \rangle = \mathcal{L}_\rho^2 \left\langle \frac{\partial \rho}{\partial z} \right\rangle \left\langle \frac{\partial u}{\partial z} \right\rangle \tag{12}$$

In figure 10, both parametrizations for the Reynolds stress equations (9) and (11), respectively (a,c), and for the buoyancy turbulent fluxes as given in equations (10) and (12), respectively, (b,d), are reported. Two-dimensional

411 histograms show the correlation between fluxes and gradients, but no con-
412 vergence for both models is found.

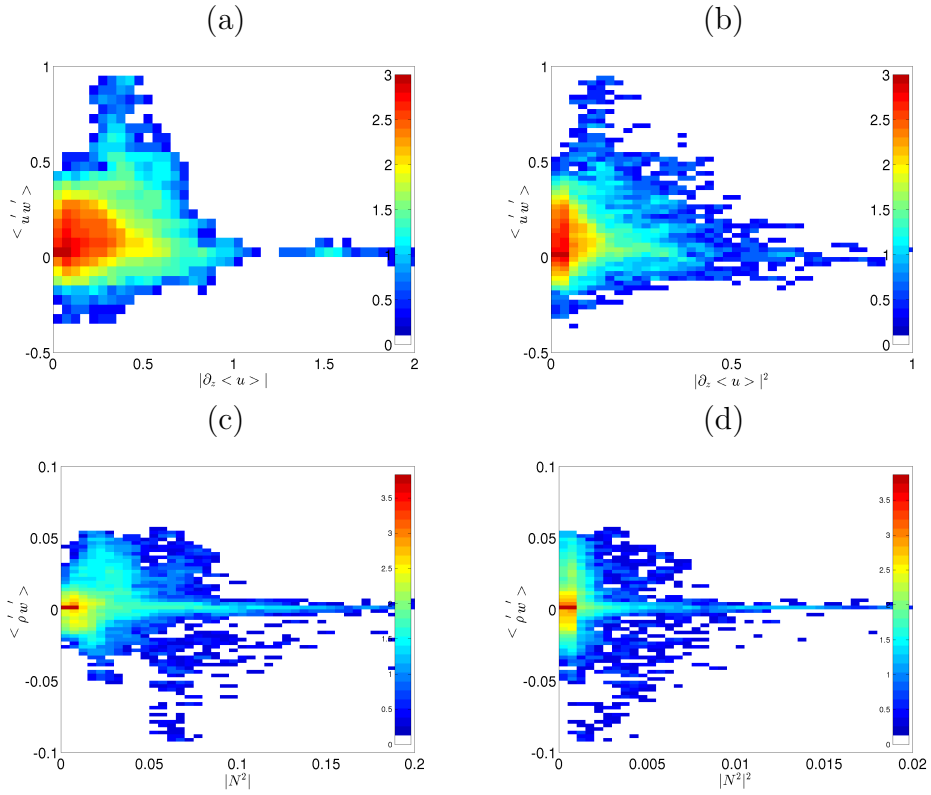

Figure 10: Two-dimensional histograms representing the correlation between the Reynolds stress and the mean gradients. The color scale represents the $\log_{10}$ number of entries in the histogram. (a) Momentum flux $\langle u'w' \rangle$ versus the vertical-velocity gradient $\langle \partial u/\partial z \rangle$ and (b) versus the square of the velocity vertical gradient $\langle \partial u/\partial z \rangle^2$. (c) Buoyancy flux $\langle \rho'w' \rangle$ versus the vertical density gradient expressed using the Brunt Väisälaa frequency N^2 and (d) versus the square $(N^2)^2$.

413 Thorpe (1977) proposed a characteristic length scale related to a density
414 profile in a mixed patch, obtained by adiabatically re-ordering the density
415 profile in the unstable regions of the water column and estimating the vertical
416 displacements Δz needed for a fluid particle to be moved from the synthetic
417 stable profile to the observed profile.

A characteristic length scale for the mixing can then be introduced from the root mean square of the vertical displacements Δz over the vertical profile

of the buoyancy cloud such as $\mathcal{L}_T = \sqrt{\overline{(\Delta z)^2}}$, where $\bar{\cdot}$ corresponds to the vertical average operator. Dillon (1980) showed that this length scale can be related to the Ozmidov scale $\mathcal{L}_O$ as

$$\mathcal{L}_O = 0.8\mathcal{L}_T, \tag{13}$$

where the Ozmidov scale $\mathcal{L}_O$ is defined as $\mathcal{L}_O = \epsilon^{1/2}N^{-3/2}$. Herein, ϵ the dissipation rate and N the Brunt-Väisälä frequency. By combining the equation (13) with the expression of $\mathcal{L}_O$ given above, the dissipation rate can be written as:

$$\epsilon = 0.64\mathcal{L}_T^2 N^3. \tag{14}$$

Osborn (1980) showed that the turbulent diffusivity is limited by the dissipation rate following the equation

$$K_\rho = -\frac{\langle w'\rho' \rangle}{\langle \partial_z \rho \rangle} \leq 0.2\epsilon/N^2 \simeq 0.13\mathcal{L}_T^2 N. \tag{15}$$

Barry et al. (2001) proposed also two equations to estimate the turbulent diffusivity depending of the buoyancy Reynolds number $Re_b = \epsilon/(\nu N^2) = 0.64\mathcal{L}_T^2 N/\nu$

$$K_\rho = \begin{cases} 0.9(\nu^2 K_{mol})^{1/3} Re_b & \text{for } 10 < Re_b < 300, \\ 24(\nu^2 K_{mol})^{1/3} Re_b^{1/3} & \text{for } Re_b > 300, \end{cases} \tag{16}$$

where K_{mol} is the molecular diffusivity of salt in water. Combining the equations (14) and (16) leads to

$$K_\rho \simeq \begin{cases} 0.6(Pr)^{-1/3}\mathcal{L}_T^2 N & \text{for } 10 < Re_b < 300, \\ 21(L_T^2 N\nu^2/Pr)^{1/3} & \text{for } Re_b > 300, \end{cases} \tag{17}$$

where $Pr = \nu/K_{mol}$ is the Prandtl number of the fluid.

Figure 11a displays the turbulent diffusivity deduced using the Thorpe scale $\mathcal{L}_T$. The light-gray dots are estimated following the Osborn equation (15) and the red dashed-line is the vertical running mean of these points with a window size of $0.05z/H$. The black dots are estimated following the Barry et al. (2001) equations (17) and the red line is the vertical running mean of these points with a window size of $0.05z/H$. The vertical green line is the vertical average of the diapycnal turbulent diffusivity following Barry et al. (2001).

In figure 11b the turbulent diffusivity is estimated using equation (10) (black stars), where the continuous vertical green line represents the vertical average. Both methods (figure 11(a,b)) give a similar distribution with the same order of magnitude.

These results suggest that neither the mixing model based on the Prandtl scale $\mathcal{L}$ nor the model based on the Thorpe scale $\mathcal{L}_T$ deliver a reliable relation to parametrize turbulent fluxes.

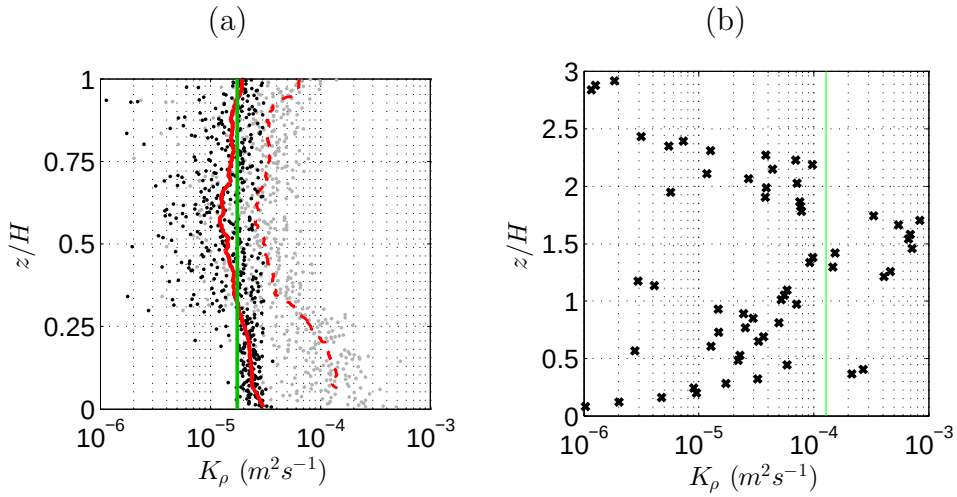

Figure 11: Diapycnal turbulent diffusivity K_ρ (m^2/s) from an instantaneous vertical density profile at the back of the buoyancy cloud using (a) The light-gray dots are estimated following the Osborn equation (15) and the red dashed-line is the vertical running mean of these points with a window size of $0.05z/H$. The black dots are estimated following the Barry et al. (2001) equations (17) and the red line is the vertical running mean of these points with a window size of $0.05z/H$. The vertical green line is the vertical average of the diapycnal turbulent diffusivity following Barry et al. (2001). (b) K_ρ estimated from equation (10) (black stars) and the associated vertical average (vertical green line).

6. Summary and conclusions

An experimental investigation of finite volume gravity currents down a slope released from a lock has been performed using combined PIV and PLIF measurement techniques to obtain two-dimensional velocity and density fields.

Experiments were focused on the deceleration region of the buoyancy cloud at a distance $x > 10H_0$ from the initial volume reservoir. Based on

the high resolved simultaneous velocity-density data, it is verified that the existing theoretical models of Beghin et al. (1981); Dai (2013a); Maxworthy (2010) are suitable for predicting the global characteristics of the cloud propagation (front propagation, lateral surface and buoyancy), with exception of the buoyancy variations that have to be corrected from Maxworthy (2010) using the coefficients given in the theoretical model of Dai (2013a).

The measurements showed the complex turbulent structure of the cloud with the back of the buoyancy cloud being hydrostatically unstable with the associated Thorpe scale larger than at the front of the cloud. Large patches of ambient fluid are engulfed into the cloud, especially at the back of the head due to a large scale recirculation vortex, that causes convectively unstable small-scale structures within the head and subsequent intense dilution. Smaller scale instabilities at the limiting edge between the head and the ambient fluid also contributes to local mixing and dilution, such as Kelvin-Helmholtz instabilities.

Using the combined velocity and density data and by averaging the buoyancy cloud along its descent, turbulent fluxes has been estimated revealing that the usual parameterization laws based on the assumption of a constant turbulent diffusivity or a constant turbulent mixing length do not work properly. These results apply for lock-release density clouds propagating down steep slopes, and in particular for the head of the gravity current, which present high spatial and temporal hetereogenity. The tail behind the passage of the head in case of continuous supply, or even some lock released gravity currents propagating on horizontal boundaries, has shown to be rather stationary and homogeneous, present self-similarity and can be treated with a good approximation as a stratified shear layer, as given by the measurements of Odier et al. (2012, 2014). The turbulent closure models based on mixing length scales (e.g. Prandtl 1925) revealed to work reasonably well in such cases. Spatial hetereogenity has been also reported for spatially developing gravity currents (Martin et al., 2019; Negretti et al., 2017). In this latter case however, turbulent diffusivities can be defined distinctively in the defined spatial regions, that can be identified using for example the internal Froude number or the bulk Richardson number (a study is currently in progress on this aspect).

The high spatio-temporal anisotropy of downslope density clouds over steep slopes makes it challenging to find a correct parametrization using closure models based on the turbulent viscosity ν_t that depend on the spatial variables. Our results show clearly that none of the parametrizations

proposed in the literature can properly represent turbulent diffusivities for downslope propagating density clouds. The fact that in figure 10 the histograms show no correlation between the turbulent fluxes and a mixing length, the strong vertical variations shown in figure 11 using the formulation of Osborn (1980) and Barry et al. (2001), comes from the fact that for downslope propagating buoyancy clouds over steep slopes there are several characteristic scales, which are set by the multiplicity of turbulent processes that take place, along with their intermittency. These are convective unstable processes (inside the cloud), Kelvin-Helmholtz (shear) instabilities (at the edge with the ambient fluid) and lobes and clefts instabilities (not observed in this study). Under these conditions, mixing scales go from the small convectively unstable scales, the Kelvin-Helmholtz scales, up to the large scale recirculation vortex, which is of the same order of the size of the cloud itself, as also highlighted in figure 9.

The parametrization of the turbulent diffusivities should be based rather on scalar quantities that avoid the problem of spatial hetereogenity and takes into account the different sources of turbulence production. This could be done for example using energetic considerations that compare the terms having a definite exchange of energy and acts as a source or a sink: the shear production deriving its energy from the mean flow (P_k), the buoyancy production representing the rate at which turbulent kinetic energy is consumed in mixing, but also aliments the production of kinetic energy for downslope propagating currents (P_b), and the viscous dissipation of turbulent kinetic energy (ϵ), governed by the balance $P_k + P_b = \epsilon$. Each of these three terms, can be represented by a characteristic length scale of shear ($\mathcal{L}_s$), of buoyancy, as for example the Monin-Obukhov or the Ozmidov scales ($\mathcal{L}_O$) and a dissipation scale ($\mathcal{L}_\epsilon$), as proposed earlier in Bradshaw (1969).

The use of the energy budget approach has also the advantage to permit extending the results to similarly spatially hetereogeneous non-conservative currents such as turbidity currents or katabatic flows, where the additional source/sink of buoyancy can be added following the suspension/deposition of fluid particles - in turbidity currents - or the presence of a local thermal flux in katabatic flows.

Additional investigations are needed to test the appropriate turbulent closure for these flows based on the above described energy approach, which is left for future work.

Declarations

The authors declare that they have no known competing financial interests or personal relationships that could have appeared to influence the work reported in this paper.

Acknowledgements

This work has been supported by the LabEx Tec 21 (Investissements d'Avenir - grant agreement n°ANR-11-LABX-0030). We are grateful to A. Di Rienzo for her support in conducting the experiments. Special thanks go to H. Bellot, C. Eymond-Gris, M. Lagauzère, L. Vignal, S. Viboud, T. Valran for technical support in the experiments. Special thanks go to E.J. Hopfinger, C. Staquet and M. Rastello for useful discussions.

Appendix A. PLIF calibration

Optical flow diagnostics techniques in a stratified environment require closely matching the refraction indices of the dense and light fluids. This is generally achieved by the use of salt water for the heavy fluid and ethanol water mixture for the light fluid. However, as shown by Daviero et al (2001), the refractive index variations in stratified flows can be neglected if the salt and dye concentrations remain below thresholds values ($\Delta\rho < 20\ kgm^{-3}, c_0 < 70\ \mu g/l$), which is the case in our study with $\Delta\rho = 5\ kgm^{-3}, c_0 = 5\ \mu g/l$.

For an excitation illumination $I_0(r, \beta)$, with (r, β) being the position along a radius and an angle of the laser sheet, and with no absorption along the laser path, there is a linear relationship between the intensity of fluorescence emission and the dye concentration, consistent with our measurements at dye concentrations ranging from 0 to 53.8 μg/l. For low laser intensities (Crimaldi, 2008), the pixel grey scale values at each location in the fluorescence image, $g_0(r, \beta, t)$, are linearly related to the dye concentration at that location, $c(r, \beta, t)$, and to $I_0(r, \beta)$ via

$$g_0(r, \beta, c) = \Gamma I_0(r, \beta) c(r, \beta, t) + g_b(r, \beta), \tag{A.1}$$

where $g_b(r, \beta)$ is the background noise or camera dark-response. The constant Γ accounts for the system-specific optical collection efficiency and the effective quantum yield of the fluorescent dye. Here the subscript '0' denotes the case without absorption. The values of $\Gamma I_0(r, \beta)$ and $g_b(r, \beta)$ are determined from a calibration procedure detailed below.

When laser light passes through the test section, the dye solution attenuates the laser intensity and this attenuation must be corrected to obtain accurate dye concentrations from PLIF images (e.g., Atsavapranee and Gharib, 1997; Ferrier et al., 1993; Krug et al., 2013; Odier et al., 2014). In the present set-up, the propagation of the laser sheet in the field of view is along the r axis. According to the Bouguer–Lambert–Beer law, the laser intensity in such an absorbing medium is

$$I(r,\beta,t) = I_0(r,\beta)\alpha(r,\beta,c) \tag{A.2}$$

with

$$\begin{aligned} \alpha &= \exp\left(-\left(a_w r + \epsilon \int_0^r c(r',\beta,t)dr' + \epsilon_s \int_0^r c_s(r',\beta,t)dr'\right)\right) \\ &= \exp\left(-\left(a_w r + \left(\epsilon + \epsilon_s \frac{c_{s,0}}{c_0}\right)\int_0^r c(r',\beta,t)dr'\right)\right) \end{aligned} \tag{A.3}$$

where $\alpha = \alpha(r,\beta,c)$ is the attenuation along ray paths due to solution absorption. a_w is the clear water attenuation coefficient, ϵ is the attenuation coefficient of the dyed solution per unit concentration, ϵ_s is the attenuation coefficient of the salt solution per unit of salinity and $c_s(r',\beta,t)$ is the salt concentration of the water. The recorded greyscale value is then $g(r,\beta,c) = \Gamma I(r,\beta,c)c(r,\beta,t) + g_b(r,\beta)$. Substituting eq. (A.2) into this last equation leads to

$$g(r,\beta,c) = \Gamma I_0(r,\beta)\alpha(r,\beta,c)c(r,\beta,t) + g_b(r,\beta). \tag{A.4}$$

The PLIF calibration was done before and after each experiment. The main tank was filled with Rhodamine 6G with uniform known concentrations ($c = 0$, 3.8, 7.7, 15.4, 30.8, 38.5, 46.2 and 53.8 μg/l). The zero concentration measurement gives the camera dark-response $g_b(r,\beta)$. For uniform known concentrations c and for a given angle β, equation (A.4) gives

$$g(r,c)_\beta - g_b(r)_\beta = \Gamma I_0(r)_\beta \exp[1-(\epsilon c + a_w)r]c, \tag{A.5}$$

where $g_b(r)_\beta = g(r)_\beta|_{c=0}$. For $(\epsilon c + a_w)r \ll 1$ and assuming $I_0(r)_\beta \approx A_\beta r^{-1}$ far from the laser source, with A_β being a constant to be determined, the previous equation can be approximated by the following equation

$$g(r,c)_\beta - g_b(r,c)_\beta \approx \Gamma A_\beta r^{-1}\left[1-(\epsilon c + a_w)r\right]c. \tag{A.6}$$

For each angle β, a non-linear fit of equation (A.6) has been performed to find the parameters ϵ, a_w, and ΓA_β. The following attenuation coefficients has been found: $a_w = 2.8 \pm 1.7 \times 10^{-3}$ cm^{-1}, $\epsilon = 3.2 \pm 0.3 \times 10^{-4}$ (cm μg/l)$^{-1}$ and $\left(\epsilon_s \frac{c_{s,0}}{c_0}\right) \approx 1.4 \times 10^{-6}$ (cm μg/l)$^{-1} \ll \epsilon$.

Finally, the non-dimensional dynamic density is related to the measured dye concentration by $\tilde{\rho}(r, \beta, t) = c(r, \beta, t)/c_0$.

References

Adduce, C., Sciortino, G., Proietti, S., 2012. Gravity currents produced by lock-exchanges: experiments and simulations with a two layer shallow-water model with entrainment. J. Hydr. Eng. 138, 111–21.

Agrawal, T., Ramesh, B., Zimmerman, S., Philip, J., Klewicki, J.C., 2021. Probing the high mixing efficiency events in a lock-exchange flow through simultaneous velocity and temperature measurements. Phys. Fluids 33, 016605. doi:10.1063/5.0033463.

Atsavapranee, P., Gharib, M., 1997. Structures in stratified plane mixing layers and the effects of cross-shear. J. Fluid Mech. 342, 53–86.

Baines, P., 2002. Two-dimensional plumes in stratified environments. J. Fluid Mech. 471, 315–337.

Balasubramanian, S., Zhong, Q., 2018. Entrainment and mixing in lock-exchange gravity currents using simultaneous velocity-density measurements. Phys. Fluids 30, 056601. doi:10.1063/1.5023033.

Baringer, M., Price, J., 2001. Mixing and spreading of the Mediterranean outflow. J. Phys. Ocean. 27, 1654–77.

Barry, M.E., Ivey, G.N., Winters, K.B., Imberger, J., 2001. Measurements of diapycnal diffusivities in stratified fluids. J. Fluid Mech. 442, 267.

Beghin, P., Brugnot, G., 1983. Contribution of theoretical and experimental results to powder-snow avalanche dynamics. Cold Regions Science and Technology 8, 67–73.

Beghin, P., Hopfinger, E., Britter, R., 1981. Gravitational convection from instantaneous sources on inclined boundaries. J. Fluid Mech. 107, 407–422.

Bradshaw, P., 1969. Effects of streamline curvature and buoyancy in turbulent shear flow. J. Fluid Mech. 36(1), 177–91.

Britter, R., Linden, P., 1980. The motion of the front of a gravity current travelling down an incline. J. Fluid Mech. 99, 531–543.

Brun, C., 2017. Large-eddy simulation of a katabatic jet along a convexly curved slope: 2. evidence of gortler vortices. J. Geophys. Res.: Atmospheres 122, 5190–210. doi:https://doi.org/10.1002/2016JD025416.

Bründl, M., Bartelt, P., Schweizer, J., Keiler, M., Glade, T., 2010. Review and future challenges in snow avalanche risk analysis. Geomorphological hazards and disaster prevention. Cambridge University Press, Cambridge , 49–61.

Calgaro, C., Creusé, E., Goudon, T., 2015. Modeling and simulation of mixture flows: Application to powder–snow avalanches. Computers & Fluids 107, 100–122.

Charrondiere, C., Brun, C., Sicart, J., Cohard, J.M., Biron, R., Blein, S., 2020. Buoyancy effects in the turbulence kinetic energy budget and reynolds stress budget for a katabatic jet over a steep alpine slope. Boundary-Layer Meteorol. 177, 97–122.

Clément-Rastello, M., 2001. A study on the size of snow particles in powder-snow avalanches. Annals of Glaciology 32, 259–262.

Crimaldi, J., 2008. Planar laser induced fluorescence in aqueous flows. Exp. Fluids 44, 851–863.

Dai, A., 2012. Gravity currents propagating on sloping boundaries. Journal of Hydraulic Engineering 139, 593–601.

Dai, A., 2013a. Experiments on gravity currents propagating on different bottom slopes. J. Fluid Mech. 731, 117–141.

Dai, A., 2013b. Gravity currents propagating on sloping boundaries. Journal of Hydraulic Engineering 139, 593–601.

Dai, A., 2013c. Power-law for gravity currents on slopes in the deceleration phase. Dyn. Atm. Oceans 63, 94–102.

Dai, A., 2014. Non-Boussinesq gravity currents propagating on different bottom slopes. J. Fluid Mech. 741, 658–680.

Dai, A., 2015. High-resolution simulations of downslope gravity currents in the acceleration phase. Phys. Fluids 27, 076602.

Dai, A., Ozdemir, C., Cantero, M., Balachandar, S., 2011. Gravity currents from instantaneous sources down a slope. J. Hydr. Eng. 138, 237–246.

Escudier, M.P., Maxworthy, T., 1973. On the motion of turbulent thermals. J. Fluid Mech. 61, 541–552. doi:10.1017/S0022112073000856.

Étienne, J., Saramito, P., Hopfinger, E.J., 2004. Numerical simulations of dense clouds on steep slopes: application to powder-snow avalanches. Annals of Glaciology 38, 379–383.

Ferrier, A., Funk, D., Roberts, P., 1993. Application of optical techniques to the study of plumes in stratified fluids. Dyn. Atm. Oceans 20, 155–183.

Hallworth, M.A., Huppert, H.E., Phillips, J.C., Sparks, R.S.J., 1996. Entrainment into two-dimensional and axisymmetric turbulent gravity currents. J. Fluid Mech. 308, 289–311.

Hampton, M.A., 1972. The role of subaqueous debris flow in generating turbidity currents. J. Sedim. Res.h 42.

Holyer, J., Huppert, H., 1980. Gravity currents entering a two-layer fluid. J. Fluid Mech. 100, 739–767.

Hopfinger, E., 1983. Snow avalanche motion and related phenomena. Ann. Rev. Fluid Mech. 15, 47–76.

Hopfinger, E., Tochon-Danguy, J.C., 1977. A model study of powder-snow avalanches. J. Glaciol. 19, 343–356.

Hoult, D., 1972. Oil spreading on the sea. Annu. Rev. Fluid Mech. 4, 341–368.

Huppert, H., Simpson, J., 1980. The slumping of gravity currents. J. Fluid Mech. 99, 785–799.

Kostaschuk, R., Nasr-Azadani, M.M., Meiburg, E., Wei, T., Chen, Z., Negretti, M.E., Best, J., Peakall, J., Parsons, D., 2018. On the causes of pulsing in continuous turbidity currents. J. Geophys. Res: Earth Surface 123, 2827–2843. doi:https://doi.org/10.1029/2018JF004719.

Krug, D., Holzner, M., Lüthi, B., Wolf, M., Kinzelbach, W., Tsinober, A., 2013. Experimental study of entrainment and interface dynamics in a gravity current. Exp. in fluids 54, 1530.

Madec, G.e.a., 2015. Nemo ocean engine, Notes du Pole de modelisation de l'Institut Pierre-Simon Laplace (IPSL).

Marino, B., Thomas, L., Linden, P., 2005. The front condition for gravity currents. J. Fluid Mech. 536, 49–78.

Martin, A., Negretti, M.E., Hopfinger, E.J., 2019. Development of gravity currents on slopes under different interfacial instability conditions. J. Fluid Mech. 880, 180–208.

Martin, A., Negretti, M.E., Ungarish, M., Zemach, T., 2020. Propagation of a continuously supplied gravity current head down bottom slopes. Phys. Rev. Fluids 5, 054801.

Martin, J.E., García, M.H., 2009. Combined piv/plif measurements of a steady density current front. Exp. Fluids 46, 265–276.

Maxworthy, T., 2010. Experiments on gravity currents propagating down slopes. part 2. the evolution of a fixed volume of fluid released from closed locks into a long, open channel. J. Fluid Mech. 647, 27–51.

Maxworthy, T., Nokes, R., 2007. Experiments on gravity currents propagating down slopes. part 1. the release of a fixed volume of heavy fluid from an enclosed lock into an open channel. J. Fluid Mech. 584, 433–453.

Meiburg, E., Kneller, B., 2010. Turbidity currents and their deposits. Ann. Rev. Fluid Mech. 42, 135–156.

Morton, B., Taylor, G., Turner, J., 1956. Turbulent gravitational convection from maintained and instantaneous sources. Proc. R. Soc. Lond. A2341, 23.

Mukherjee, P., Balasubramanian, S., 2020. Energetics and mixing efficiency of lock-exchange gravity currents using simultaneous velocity and density fields. Phys. Rev. Fluids 5, 063802.

Mukherjee, P., Balasubramanian, S., 2021. Diapycnal mixing efficiency in lock-exchange gravity currents. Phys. Rev. Fluids 6, 013801.

Negretti, M.E., Flòr, J.B., Hopfinger, E.J., 2017. Development of gravity currents on rapidly changing slopes. J. Fluid Mech. 833, 70–97.

Nishimura, K., Ito, Y., 1997. Velocity distribution in snow avalanches. J. Geophys. Res: Solid Earth 102, 27297–27303.

Odier, P., Chen, J., Ecke, R., 2012. Understanding and modeling turbulent fluxes and entrainment in a gravity current. Physica D: Nonlinear Phenomena 241, 260–268.

Odier, P., Chen, J., Ecke, R.E., 2014. Entrainment and mixing in a laboratory model of oceanic overflow. J. Fluid Mech. 746, 498–535.

Osborn, T., 1980. Estimates of the local rate of vertical diffusion from dissipation measurements. J. Phys. Ocean. 10, 83–9.

Ottolenghi, L., Cenedese, C., Adduce, C., 2017. Entrainment in a dense current flowing down a rough sloping bottom in a rotating fluid. J. of Phys. Oceanogr. 47, 485–498.

Pelmard, J., S., N., Friedrich, H., 2021. Turbulent density transport in the mixing layer of an unsteady gravity current. Advances in Water Resources , 103963doi:https://doi.org/10.1016/j.advwatres.2021.103963.

Pohl, F., Eggenhuisen, J.T., Kane, I.A., Clare, M.A., 2020. Transport and burial of microplastics in deep-marine sediments by turbidity currents. Environmental Science & Technology .

Prandtl, L., 1925. Bericht über die entstehung der turbulenz. Z. Angew. Math. Mech 5, 136–139.

Rastello, M., Hopfinger, E.J., 2004. Sediment-entraining suspension clouds: a model of powder-snow avalanches. J. Fluid Mech. 509, 181–206.

Ross, A.N., Linden, P., Dalziel, S.B., 2002. A study of three-dimensional gravity currents on a uniform slope. Journal of Fluid Mechanics 453, 239–261.

Simpson, J.S., 1982. Gravity currents in the laboratory, atmosphere and ocean. Ann. Rev. Fluid Mech. 14, 213–234.

Steenhauer, K., Tokyay, T., Constantinescu, G., 2017a. Dynamics and structure of planar gravity currents propagating down an inclined surface. Phys. Fluids 29, 036604.

Steenhauer, K., Tokyay, T., Constantinescu, G., 2017b. Dynamics and structure of planar gravity currents propagating down an inclined surface. Phys. Fluids 29, 036604.

Thomas, L., Dalziel, S., Marino, B., 2003. The structure of the head of an inertial gravity current determined by particle-tracking velocimetry. Exp. Fluids 34, 708–716.

Thorez, S., Blanckaert, K., Lemmin, U., Barry, D.A., 2021. From inflow to interflow, through plunging and lofting: Uncovering the dominant flow processes of a sediment-rich negatively buoyant river inflow into a stratified lake. EGU21 13214, 19–30. doi:10.5194/egusphere-egu21-13214.

Thorpe, S., 1977. Turbulence and mixing in a scottish loch. Philos. Trans. R. Soc. London A286, 125–81.

Tickle, G., 1996. A model of the motion and dilution of a heavy gas cloud released on a uniform slope in calm conditions. J. Hazardous Materials 49, 29–47.

Troy, C., Koseff, J., 2005. The generation and quantitative visualization of breaking internal waves. Exp. Fluids 38, 549–562.

Ungarish, M., 2009. An introduction to gravity currents and intrusions, Chapman and Hall/CRC, p. 513.

Webber, D., Jones, S., Martin, D., 1993. A model of the motion of a heavy gas cloud released on a uniform slope. J. Hazardous Materials 33, 101–22.

720 Zemach, T., Ungarish, M., Martin, A., Negretti, M.E., 2019. On gravity
721 currents of fixed volume that encounter a down-slope or up-slope bottom.
722 Phys. Fluids 31, 096604.